Journal for ImmunoTherapy of Cancer

Methylglyoxal from gut microbes boosts radiosensitivity and radioimmunotherapy in rectal cancer by triggering endoplasmic reticulum stress and cGAS-STING activation

Han Zhou ,[1,2] Lei Wang,[3] Zhiwen Lin,[4,5] Chenwei Jiang,[6] Xingte Chen,[1] Kai Wang,[7] Libin Liu,[1] Lingdong Shao,[1] Jianji Pan,[1] Jinluan Li,[1] Da Zhang,[4] Junxin Wu[1]

To cite: Zhou H, Wang L, Lin Z, *et al*. Methylglyoxal from gut microbes boosts radiosensitivity and radioimmunotherapy in rectal cancer by triggering endoplasmic reticulum stress and cGAS-STING activation. *Journal for ImmunoTherapy of Cancer* 2023;**11**:e007840. doi:10.1136/jitc-2023-007840

► Additional supplemental material is published online only. To view, please visit the journal online (http://dx.doi.org/10.1136/jitc-2023-007840).

HZ, LW and ZL are joint first authors.

Accepted 10 November 2023

For numbered affiliations see end of article.

Correspondence to
Professor Junxin Wu;
junxinwufj@aliyun.com

Prof. Da Zhang;
zdluoman1987@163.com

ABSTRACT

Background Preoperative radiation therapy (preRT) is a fundamental aspect of neoadjuvant treatment for rectal cancer (RC), but the response to this treatment remains unsatisfactory. The combination of radiation therapy (RT) and immunotherapy (iRT) presents a promising approach to cancer treatment, though the underlying mechanisms are not yet fully understood. The gut microbiota may influence the response to RT and immunotherapy. Therefore, we aimed to identify the metabolism of gut microbiota to reverse radioresistance and enhance the efficacy of iRT.

Methods Fecal and serum samples were prospectively collected from patients with locally advanced rectal cancer (LARC) who had undergone pre-RT treatment. Candidate gut microbiome-derived metabolites linked with radiosensitization were screened using 16s rRNA gene sequencing and ultrahigh-performance liquid chromatography-mass coupled with mass spectrometry. In vitro and in vivo studies were conducted to assess the radiosensitizing effects of the metabolites including the syngeneic CT26 tumor model and HCT116 xenograft tumor model, transcriptomics and immunofluorescence. The CT26 abscopal effect modeling was employed to evaluate the combined effects of metabolites on iRT.

Results We initially discovered the gut microbiota-associated metabolite, methylglyoxal (MG), which accurately predicts the response to preRT (Area Under Curve (AUC) value of 0.856) among patients with LARC. Subsequently, we observed that MG amplifies the RT response in RC by stimulating intracellular reactive oxygen species (ROS) and reducing hypoxia in the tumor in vitro and in vivo. Additionally, our study demonstrated that MG amplifies the RT-induced activation of the cyclic guanosine monophosphate AMP synthase-stimulator of interferon genes pathway by elevating DNA double-strand breaks. Moreover, it facilitates immunogenic cell death generated by ROS-mediated endoplasmic reticulum stress, consequently leading to an increase in $CD8^+$ T and natural killer cells infiltrated in the tumor immune microenvironment. Lastly, we discovered that the combination of anti-programmed cell death protein 1 (anti-PD1) therapy produced long-lasting complete responses in all irradiated tumor sites and half of the non-irradiated ones.

Conclusions Our research indicates that MG shows promise as a radiosensitizer and immunomodulator for RC. Furthermore, we propose that combining MG with iRT has great potential for clinical practice.

WHAT IS ALREADY KNOWN ON THIS TOPIC

⇒ The response to preoperative radiotherapy in patients with locally advanced rectal cancer is not influenced by gut microbiota. However, the efficacy of immunotherapy (iRT) is affected by gut microbiota.

WHAT THIS STUDY ADDS

⇒ In this present study, we have discovered a microbiota called methylglyoxal (MG), which is derived from the gut microbiota. We found that MG can enhance the radiosensitivity of rectal cancer (RC) by increasing the levels of reactive oxygen species within cells and reducing tumor hypoxia. In addition, the combination of MG and radiation therapy (RT) has the potential to alter the tumor immune microenvironment (TiME) through the induction of immunogenic cell death, and activation of the cyclic guanosine monophosphate AMP synthase (cGAS)-stimulator of interferon genes (STING) pathway. Furthermore, the combination of RT, MG and anti-PD1 therapy has the potential to achieve effective local control and an enhanced abscopal effect in patients with RC.

HOW THIS STUDY MIGHT AFFECT RESEARCH, PRACTICE, OR POLICY

⇒ This study offers novel insights into the potential of gut microbiota-derived metabolites for use as the radiosensitizers and regulators of the TiME combined with RT. In addition, this study also highlights the potential of MG in conjunction with iRT to bolster an immune response against tumors and improve treatment outcomes for RC.

BACKGROUND

Radiotherapy (RT) is commonly used as a neoadjuvant approach for locally advanced rectal cancer (LARC) with or without chemotherapy.[1] Nonetheless, responses to RT among patients reveal significant heterogeneity, with pathological complete response (pCR) rates ranging from 6% to 39%.[2–5] In addition, a considerable proportion of patients with LARC (20%–40%) do not respond to preoperative RT (preRT).[6 7] Studies have shown that hypoxia can induce transcription through hypoxia-inducible factor (HIF)-1α, reprogram energy metabolism, upregulate genes related to angiogenesis, and lead to radioresistance.[8 9] Thus, it is crucial to alleviate hypoxia within the tumor to reverse radioresistance.

Immune checkpoint inhibitors (ICIs) have shown promise in various kinds of solid cancers with increasingly promising results.[10] However, only a small percentage of patients with colorectal cancer (CRC) with metastatic mismatch repair deficient/microsatellite instability-high are responsive to ICIs. This group accounts for 5%–10% of patients with CRC.[11] Nowadays, RT is widely recognized as a mechanism to trigger local and/or systemic immune responses, which supports the combination of RT with immunotherapy (iRT).[10 12] A phase II study involving patients with MSI-H LARC who received preRT and ICIs reported a high pCR rate of up to 50%.[13] However, there are still several unresolved questions that need attention: (1) only about 40% of patients with pan-cancer experienced a benefit from the iRT,[12] (2) the optimal dose and fraction of RT as well as the timing sequence of immunotherapy, is still unknown,[14] (3) the abscopal effect has only been observed in case reports,[15 16] and (4) the safety of combination treatment remains a concern.[10 12]

The gut microbiome is a complex community of microbes that is strongly associated with the development and progression of RC.[17] Previous studies have demonstrated the ability of the gut microbiome to predict the response to preRT, improve the treatment response and reduce the treatment toxicity.[18–20] Furthermore, it has also been confirmed that the gut microbiome can reshape the tumor immune microenvironment (TiME) and thus impact the response to ICIs.[19 21] However, direct utilization of gut microbiota in the clinic has been severely limited due to interindividual heterogeneity and their dual impact on the TiME.[21 22] Microbiota-derived metabolites serve as the connection between the microbiota and cancers.[23] With the growing understanding of microbiome-related metabolites in cancer development, research has identified several metabolites, including short-chain fatty acids[24] and hydrophobic bile acids[25] that generate reactive oxygen species (ROS) through multiple pathways. This process enhances the effectiveness of chemotherapy[26] and immunotherapy.[27] Nonetheless, only a limited number of investigations[20] have been undertaken to explore the effect of gut microbiome-derived metabolites in the response to RT.

In this study, using 16s rRNA gene sequencing and ultrahigh-performance liquid chromatography-mass coupled with mass spectrometry (UHPLC-MS/MS) analysis, we first identified a gut microbiota-derived metabolite, methylglyoxal (MG), which can predict the preRT response in a cohort of 26 patients with LARC. Then, we conducted experiments using the CT26 and HCT116 cell lines, as well as both syngeneic CT26 and HCT116 xenograft tumor models, to investigate the impact of MG on the radiosensitivity of RC in vitro and in vivo. Furthermore, we demonstrated the combination of MG and RT has significant immunomodulatory effects on the TiME by inducing immunogenic cell death (ICD) and activating the cyclic guanosine monophosphate AMP synthase (cGAS)-stimulator of interferon genes (STING) pathway. Notably, MG also enhances the treatment response and abscopal effect of iRT in a bilateral syngeneic tumor model. This combined approach resulted in a persistent complete response (CR) across all irradiated tumor sites and marked regression in 50% of the non-irradiated tumors.

METHODS

Clinical information and omics analysis

This study involved 26 patients with LARC who received preRT at Fujian Cancer Hospital from September 2020 to September 2021. Supplementary methods contained the treatment protocol, tumor regression grade (TRG) and sampling procedure. To investigate the correlation between treatment response and the gut microbiota, 16s rRNA gene sequencing was used. Metabolism was analyzed using UHPLC-MS/MS analysis, and the relationship between metabolism and gut microbiota was determined through the Spearman correlation method. The omics analysis detail was provided in the online supplemental method section.

Cell cultures and treatment

The CT26, HCT116 CRC cell lines, the DC2.4 cell line, and human umbilical vein endothelial cells (HUVEC) were obtained from the National Collection of Authenticated Cell Cultures, Shanghai Institute of Biochemistry and Biological Sciences, the Chinese Academy of Sciences. The cells were cultured in Roswell Park Memorial Institute 1640 (RPMI-1640, Gibco) supplemented with 10% fetal bovine serum (Gibco) and 1% penicillin-streptomycin (Gibco). Cells were seeded at the appropriate concentration 24 hours before treatment and divided into four groups: phosphate-buffered saline (PBS), MG, RT and RT+MG groups.

Cell viability

Cell viability was assessed using the Cell Count Kit-8 (CCK-8) assay and live/dead cell analysis. Specifically, 8×10^3 cells per well were seeded in 96-well plates and cultured for an additional 48 hours before the CCK-8 assay and the live/dead cell analysis.

Colony formation assay

For the colony formation assay, cells were seeded in 12-well plates at a density of 500 cells per well. After 7 days, the

cells were fixed with 4% paraformaldehyde, stained with crystal violet solution, and then counted using ImageJ software (V.1.51).

ROS measurement

Cells were seeded in 96-well plates following standard protocol at a density of 1×10^5 cells per well. Prior to imaging, cells were stained with a 50 µM concentration of the 2,7-dichlorofluorescein diacetate (DCFH-DA) fluorescent probe for 30 min. Fluorescence images were captured using an inverted fluorescence microscope with excitation at 488 nm.

Confocal laser scanning microscope (CLSM)

Cells were seeded in confocal dishes at a density of 1×10^5 cells per well. 6 hours after treatment, cells were fixed with 4% paraformaldehyde, blocked with 0.1% Triton solution, and then incubated with the primary antibody (online supplemental table 1) overnight at 4°C. Cells were then stained with an Alexa Fluor 647-conjugated secondary antibody and visualized by CLSM (Carl Zeiss LSM780). Details of the experimental procedures are described in the online supplemental material.

DC maturation and T-cell stimulation

Bone marrow-derived dendritic cells (DCs) were obtained from the tibia and femur bones of BALB/c mice and cultured in complete RPMI-1640 medium supplemented with 20 ng/mL granulocyte-macrophage colony stimulating factor (GM-CSF) and 10 ng/mL interleukin (IL)-4 in 24-well plates for 6 days. CT26 cells were seeded in the upper chamber and treated according to the previous report. Mature DCs (mDCs) were collected after 48 hours of co-culture with CT26 cells and then incubated with the splenic monocytes.

Tumor challenge and treatment

Female 6-week-old BALB/c mice were obtained from the Shanghai Wushi Experimental Animal Center (Shanghai, China). CT26-LUC cells were subcutaneously injected into the right hind legs of BALB/c mice at a density of 5×10^5 cells. Tumor volume = [(tumor length) × (tumor width)^2]/2. When the tumor volume reached approximately 100 mm^3, the mice were divided into four groups: PBS, MG (20 mg/kg, i.t.), RT (6 Gy), and RT+MG groups. The tumor volume was measured every 3 days. Mice were sacrificed when tumor volume reached 1500 mm^3.

Abscopal effect model and treatment

To establish an abscopal effect model, an additional injection of CT26-LUC cells was administered subcutaneously into the left hind legs of mice at a density of 2×10^5 cells per mouse 3 days after the first inoculation. Mice were then randomly assigned to the following groups: RT group with 6 Gy RT, RT+MG group with 6 Gy RT and 20 mg/kg MG (i.t.), iRT group with 6 Gy RT and 4 mg/kg α-PD1 (i.p.), and MG+iRT groups with 6 Gy RT, 20 mg/kg MG (i.t.) and 4 mg/kg α-PD1 (i.p.) before treatment. Mice were sacrificed when tumor volume reached 1500 mm^3, regardless of the irradiated or secondary tumor.

Bioluminescence in vivo imaging

Bioluminescent images were collected 10 min after injection of luciferin (Perkin Elmer, 15 mg/mL, 200 µL per mouse) by IVISSpectrum In Vivo Imaging System. The bioluminescence signals were quantified as average radiance (photons, s^{-1} cm^{-2} sr^{-1}).

Flow cytometry (FCM)

Single-cell suspensions were obtained from cultured cells or tumor tissues. Cells were first blocked with 5% bovine serum albumin (BSA) and subsequently incubated with the primary antibody (online supplemental table 2). Analysis was performed using the BD FACSVerse (BD Biosciences, USA) and the FlowJo software (V.10.6.1). Details of the experimental procedures are described in the online supplemental information.

Elisa

Cell supernatants and tissue homogenates were collected for the evaluation of cytokines levels. According to the protocol, the conjugate reagent was added to the plates incubated with samples and standard solutions. Chromogen solutions A and B were then added to the plates before analysis. After incubation for 15 min, the optical density was measured at 450 nm using the Spectro Max M5e instrument (Molecular Devices, USA). Details of the experimental procedures are described in the online supplemental information.

Western blot analysis

Proteins from tumor tissues and cells were extracted using radioimmunoprecipitation assay lysis buffer supplemented with phenylmethanesulfonyl fluoride, a protease inhibitor cocktail, and phosphatase inhibitors. After quantification using the bicinchoninic acid kit, the proteins were separated by sodium dodecyl-sulfate polyacrylamide gel electrophoresis (SDS-PAGE) and transferred to nitrocellulose membranes. The membranes were then blocked with 5% BSA and incubated with primary antibodies (online supplemental table 3), followed by secondary antibodies. Details of the experimental procedures are described in the online supplemental information.

Immunohistochemistry or immunofluorescence

Tumor tissues were first fixed in 4% paraformaldehyde, embedded in paraffin, and then sectioned. Sections were pretreated according to the protocol and then incubated with primary antibodies (online supplemental table 1) followed by secondary antibodies. Images were captured by fluorescence microscopy (Nikon A1 confocal microscope, Japan). Details of the experimental procedures are described in the online supplemental information.

Transcriptomes and bioinformatics analysis

Tumor tissues were dissected and frozen using liquid nitrogen. Following RNA extraction, transcriptome

sequencing was conducted to identify differentially expressed genes (DEGs) between the groups, using a $|\log_2 FC| \geq 1$ and $p < 0.05$ as criteria. Functional enrichment analysis was performed based on the DEGs using gene set enrichment analysis (GSEA).

Statistical analysis

A one-way analysis of variance was conducted using GraphPad Prism V.8.0 software to compare multiple groups, while a two-tailed Student's t-test was used to compare two groups and calculate p values. The Kaplan-Meier estimation method was employed to construct survival curves, and the log-rank test was used for testing. P values below 0.05 are regarded as statistically significant (*p<0.05, **p<0.01, ***p<0.001). Numerical data from a minimum of three independent experiments are presented as mean±SD.

RESULTS

Identification of MG to predict the response to pRT

To initiate our investigation, we prospectively collected fecal and blood samples from a group of 26 patients with LARC who underwent preRT. Subsequently, microbial genomics analysis was conducted on these samples (figure 1A). A summary of the patient's baseline characteristics and treatment response is provided in online supplemental table 4. The patients with TRG scores of 0 and 1 were designated as the sensitive group, while those with scores of TRG 2 and 3 were designated as the resistant group. The analysis of alpha diversity revealed no significant difference between the resistant group and the sensitive group at the preRT baseline (p>0.05, online supplemental figure 1). However, on employing non-metric multidimensional scaling analysis, we discerned significant disparities in species diversity between the two groups (stress=0.082, p<0.05, figure 1B). Figure 1C presents the results of the linear discriminate analysis effect size analysis, showing the differential microbiota between sensitive and resistant groups. In addition, a distinct clustering of metabolism-related signaling pathways in the sensitive group *via* predictive functional profiling of microbial communities (figure 1D). Based on these findings, we hypothesized that gut microbiota may regulate the response to preRT through their metabolites.

To further identify the metabolite responsible for regulating the preRT response, we conducted metabolite analysis on peripheral blood samples using UHPLC-MS/MS. We found a total of 21 582 metabolites (online supplemental table 5), of which 32 were identified as differential metabolites between the sensitive and resistant groups using orthogonal partial least structures-discriminant analysis (OPLS-DA). Differential metabolites were identified based on a set of criteria: variable importance in projection>1 and p<0.05 criteria (online supplemental table 6). The high credibility of the OPLS-DA model was confirmed by the permutations testing (R^2=0.85, Q^2=−0.15, figure 1E). The top 10 metabolites closely associated with preRT response are shown in figure 1F.

We performed a Spearman correlation analysis to identify the metabolites closely associated with gut microbiota and the preRT response. The heat map showed a significant association between *Lactobacillus* andMG, both of which were enriched in the sensitive group (figure 1G). In addition, both *Lactobacillus* and MG predicted preRT response, with respective AUC values of 0.751 and 0.876 (figure 1H,I). Our findings have identified a metabolite of gut microbiota, known as MG, that demonstrates a strong correlation with radiation sensitivity. We suggested that this metabolite has significant potential as a radiosensitizer for RC treatment.

MG increases radiosensitization in vitro

To eliminate the potential radiation-sensitizing effects of MG on cytotoxicity, we initially conducted in vitro cytotoxicity assays. We determined the effects of various concentrations of MG on CT26 and HCT116 cells treated for 48 hours using the CCK8 assay. Our results showed that MG reduced cell viability in a dose-dependent manner, with an IC_{50} of 671.8 µM and 682.8 µM for CT26 and HCT116, respectively (figure 2A). To ensure the low toxicity of MG as a radiation sensitizer, we selected an experimental concentration of less than 30% IC_{50} (200 µM).[28–30] We assessed the cytotoxicity of MG using DC2.4 and HUVEC cells and did not observe any apparent toxicity at a concentration of 200 µM (online supplemental figure 2).

To investigate the potential enhancement of treatment response to RT in RC, we subjected CT26 cells and HCT116 cells to MG (200 µM) pretreatment before RT (6 Gy) and assessed the resulting radiosensitization effect at 48 hours. Our CCK8 assay showed a significant reduction in cell viability of CT26 cells and clone number when treated with MG and RT, as compared with RT alone (45.79%±1.55% vs 79.34%±0.77%, p<0.05, online supplemental figure 3A) and (8.00±1.00 vs 84.33±3.79, p<0.05, figure 2B and online supplemental figure 3B). We highlight the potential benefits of combined treatment. Similar findings were observed in HCT116 cells treated with MG and RT (figure 2B, online supplemental figure 3C,D). These findings demonstrate that MG significantly enhances the radiosensitivity of RC.

In addition, a significant increase in apoptosis of CT26 cells was observed in the RT+MG group with a 1.57-fold and 5.27-fold increase in early and late apoptosis, respectively, compared with the RT group (figure 2C and online supplemental figure 4B). Similar results were also observed in HCT116 cells following treatment with RT+MG (figure 2B,D and online supplemental figure 4C). Furthermore, in the RT+MG, the expression levels of Caspase-3, cleaved Cas-3, and Bax were upregulated, whereas Bcl-2, an anti-apoptosis protein, was downregulated when compared with the other groups (figure 2E, online supplemental figure 5A,B). Although RT has the ability to cause cell apoptosis, the combined presence of

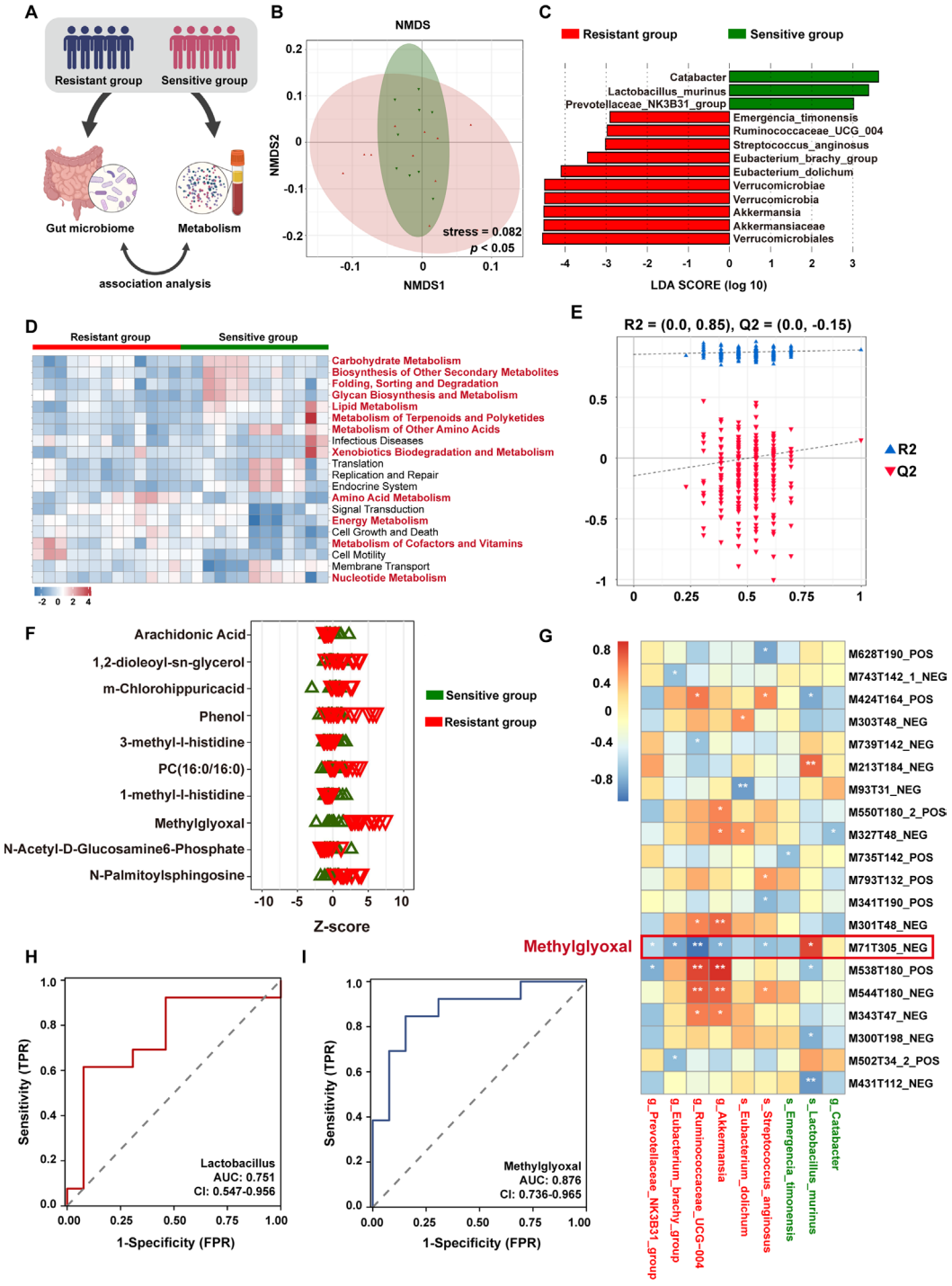

Figure 1 The gut microbiome-derived metabolite methylglyoxal (MG) impacts the effectiveness of preoperative radiotherapy (preRT) in the case of locally advanced rectal cancer (LARC). (A) Schematic of the gut microbiome and metabolite analysis. (B) Non-metric multidimensional scaling analysis was presented comparing the sensitive group and resistant group (stress=0.082, p<0.05). (C) Significant enrichment of microbiome composition in the sensitive group and resistant group based on linear discriminate analysis effect size analysis with linear discriminant analysis (LDA) score>2 and p<0.05. (D) Functional enrichment analysis of significantly different microbiomes between the sensitive group and resistant group using PICRUSt2. (E) Permutation test plot of the orthogonal partial least structures-discriminant analysis (OPLS-DA) model (R^2=0.85, Q^2=−0.15). (F) Top 10 significantly different metabolites between the two groups identified by the OPLS-DA model with variable importance in projection score>1 and p<0.05. (G) Spearman correlation heatmap displaying the relationship between significantly different microbiomes and metabolites before preRT. Receiver operating characteristic analysis is conducted of Lactobacillus (AUC=0.751) (H) and MG (AUC=0.876) (I). NMDS, non-metric multidimensional scaling.

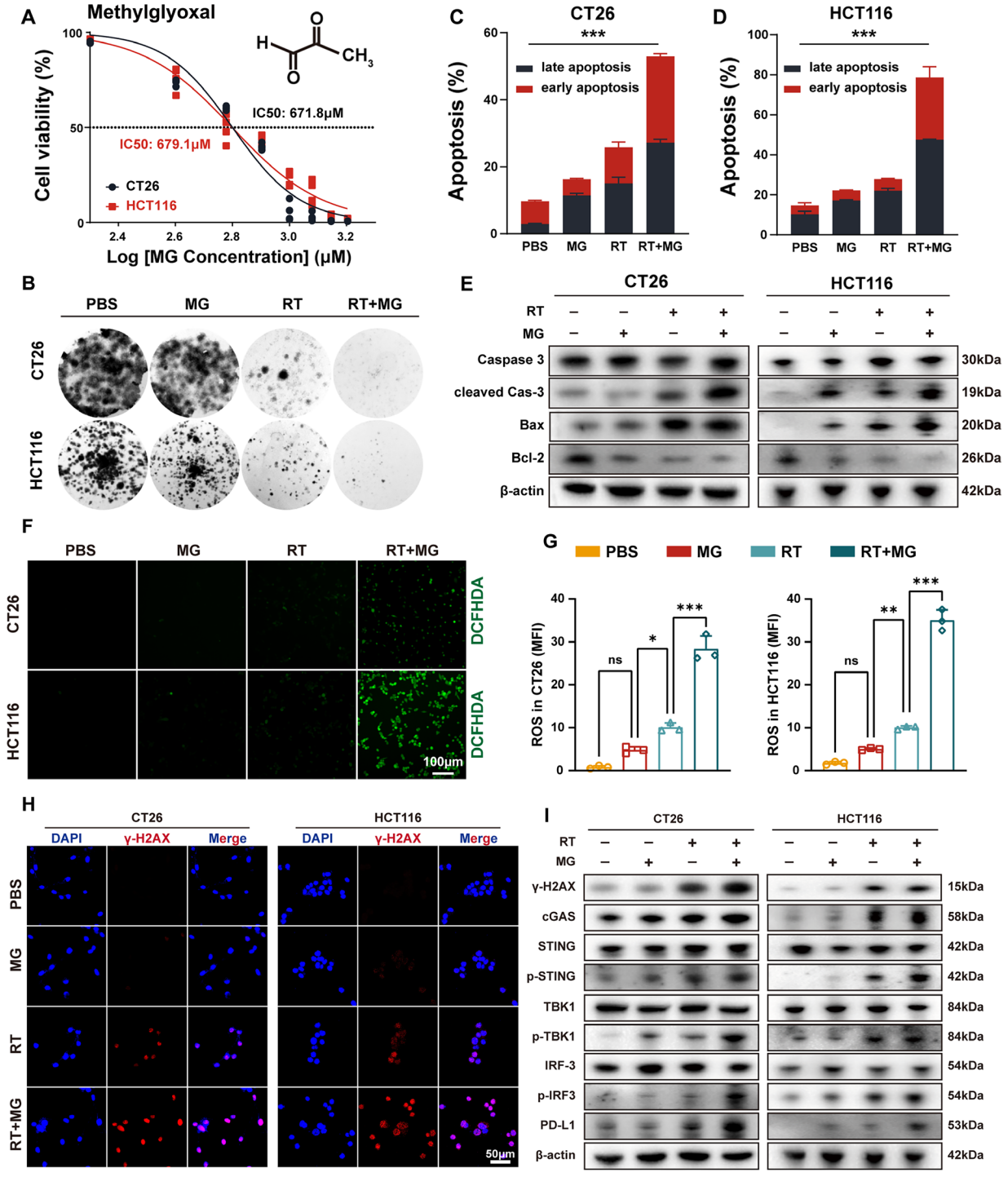

Figure 2 Effect of methylglyoxal (MG) on radiation sensitivity and activation of the cyclic guanosine monophosphate AMP synthase (cGAS)-stimulator of interferon genes (STING) pathway. (A) Determination of MG's half maximal inhibitory concentration in CT26 and HCT116 cell lines 48 hours after MG treatment (n=4). (B) Representative images showing clonal proliferation of CT26 and HCT116 cells under different treatment conditions. Quantitative analysis of early and late apoptosis rates in CT26 cells (C) and HCT116 cells (D) after coincubated with PBS and MG (200 μM) with or without X-ray (6 Gy) using flow cytometry (n=3). (E) Western blot analysis of apoptosis-related proteins expressed on the CT26 cells and HCT16 cells after coincubated with PBS and MG (200 μM) with or without X-ray (6 Gy). (F) Representative images illustrating reactive oxygen species (ROS) labeled by 2', 7'-dichlorodihydrofluorescein diacetate (DCFHDA) after coincubated with PBS and MG (200 μM) with or without X-ray (6 Gy) (scale bar, 100 μm). (G) Quantification of mean fluorescence intensity (MFI) of ROS in CT26 and HCT116 cell lines after co-incubated with PBS and MG (200 μM) with or without X-ray (6 Gy) (n=3). (H) Representative images of γ-H2AX immunofluorescence staining in CT26 and HCT116 cell lines after coincubated with PBS and MG (200 μM) with or without X-ray (6 Gy) (scale bar, 50 μm). (I) Western blot analysis of proteins related to the cGAS-STING pathway on the CT26 cells and HCT16 cells after coincubated with PBS and MG (200 μM) with or without X-ray (6 Gy). Data are presented as mean±SD. ns, no statistical difference. *p<0.05; **p<0.01; ***p<0.001.

MG enhances this effect, suggesting that the apoptosis-related proteins in CT26 cells are primarily influenced by both RT and MG. These results suggest that the combination of RT and MG provides an efficient combination therapeutic strategy for RC.

ROS has been confirmed as a crucial factor in DNA strand breaks, which is one of the classical mechanisms of radiation sensitization.[31 32] Our results indicate that combining RT with MG enhances the mean fluorescence intensity (MFI) of ROS in both CT26 and HCT116 cells compared with using RT alone. To measure ROS MFI values, we used 2',7'-dichlorodihydrofluorescein diacetate (DCFHDA), which revealed that the PBS, MG, RT and MG+RT treated groups exhibited ROS MFI values in CT26 cells. The levels of 0.82±0.33, 4.79±0.76, 10.08±1.04 and 28.31±3.06 were observed respectively, and in HCT116 cells, the levels were 1.77±0.34, 5.04±0.25, 12.06±0.37 and 35.03±2.45 (figure 2F,G). Furthermore, increased γ-H2AX staining within CT26 and HCT116 cells was detected in the RT and MG group compared with other groups, as observed by CLSM (figure 2H) and FCM (both p<0.05, online supplemental figure 6A,B). Western blot analysis has verified the upregulation of γ-H2AX in CT26 and HCT116 cells treated with RT+MG (figure 2I, online supplemental figure 7A,B). These results MG can elevate intracellular ROS, intensifying DNA strand breakage, and ultimately, augmenting radiation-induced apoptosis.

RT-induced DNA fragmentation is a classical mechanism for activating the cGAS-STING pathway.[33] Thus, we analyzed the levels of essential proteins extracted from CT26 and HCT116 cells treated with RT and MG through Western blot. Our findings revealed that CT26 and HCT116 cells treated with MG and RT have increased expressions of phosphorylated (p-) STING, TANK-binding kinase 1 (TBK1), and interferon regulatory factor 3 (IRF3), indicating the activation of the cGAS-STING pathway (figure 2I, online supplemental figure 7A,B). Furthermore, the study revealed that programmed death-ligand 1 (PD-L1), which is a downstream component of cGAS-STING,[33] was significantly overexpressed in both cell lines treated with RT+MG (figure 2I). These results confirm the activation of the cGAS- STING pathway by the combination of RT and MG and suggest the possibility of combining PD-1 inhibitors with the treatment.

MG induces ICD via endoplasmic reticulum (ER) stress pathway in vitro

Evidences have shown that ROS amplification can induce ER stress,[31 34] leading to the activation of the PKR-like ER kinase (PERK)-eukaryotic translation initiation factor 2α (eIF2α)-recombinant activating transcription factor 4 (ATF4) signaling pathway.[34] Changes in PERK, eIF2α and ATF4 levels were determined in CT26 cells and HCT116 cells treated with RT and MG using western blot analysis. As expected, level of p-PERK and eIF2α levels were increased in both CT26 and HCT116 cells after treatment with RT+MG compared with the other groups, along with increased ATF4 expression (figure 3A, online supplemental figure 8A,B). These findings suggest that the combination of RT and MG promotes ER stress and upregulates the PERK-eIF2α-ATF4 pathway.

In addition, activated ER stress can also induce ICD,[34] leading to an antitumor immune response. Calreticulin (CRT) exposure serves as an early biomarker of ICD.[32] To evaluate the CRT levels on CT26 cells and HCT116 cells surfaces following RT and MG treatment, we utilized CLSM and FCM. CLSM images demonstrated an elevated CRT exposure in both CT26 and HCT116 cells treated with RT+MG compared with the other groups (figure 3B). FCM analysis revealed that the percentage of CRT^{+} cells increased by 10.14% and 17.30% at 24 hours after post treatment in the RT+MG group of CT26 and HCT116 cells, respectively, compared with the RT group (p<0.05, online supplemental figure 9A,B). During ICD, dying cells release ATP as an additional signal.[32] We assessed intracellular and extracellular ATP levels after RT and MG treatment using an ATP assay kit. Intracellular ATP levels were reduced by 33.14% and 46.00% in the RT+MG group at 48 hours, compared with RT alone. Meanwhile, extracellular ATP levels increased by 1.31-fold and 1.60-fold in CT26 and HCT116 cells, respectively (figure 3C,D). In addition, in the late stage of ICD, high-mobility group box 1 (HMGB1) secretion is a key component.[32] HMGB1 levels were observed to increase in the RT+MG group in both CT26 and HCT116 cells when compared with the other groups (p<0.05, figure 3E,F). These findings suggest that the combination of RT and MG can enhance ICD in tumor cells.

ICD can promote the recruitment and activation of DCs[32 35] which subsequently drive T cell-mediated antitumor immune responses.[32] To activate DCs, MG treatment was initially administered to CT26 cells with or without RT treatment. Then, the bone marrow DCs were coincubated with preconditioned CT26 cells for 48 hours as previously reported,[36] following which the levels of cytokines from the supernatant were analyzed through an ELISA kit. FCM analysis showed a significant increase in mDCs within DC1s, rising from 53.77%±1.33% with RT to 67.07%±2.61% with RT+MG (p<0.05, online supplemental figure 3G,10). In addition, the RT+MG group exhibited 1.59-fold and 1.75-fold increases in tumor necrosis factor (TNF)-α and IL-12, respectively, when compared with the RT groups alone (p<0.05, figure 3H, online supplemental figure 11A,B). However, transforming growth factor (TGF)-β and IL-10 exhibited a decrease of 2.44-fold and 2.99-fold in the RT+MG group compared with the RT group (p<0.05, figure 3H, online supplemental figure 11C,D). Next, mDCs were cocultured with naive splenic T cells for 48 hours to stimulate the differentiation of cytotoxic T lymphocytes.[37] The ELISPOT assay showed a 1.48-fold increase in the number of IFN-γ spots per 10^5 cells in the RT+MG group compared with the RT group (p<0 .05, online supplemental figures 3I,J and 12). These results demonstrate that the combination of MG and RT enhances the ICD of tumor cells, leading to the activation of DC-mediated antitumor immune response.

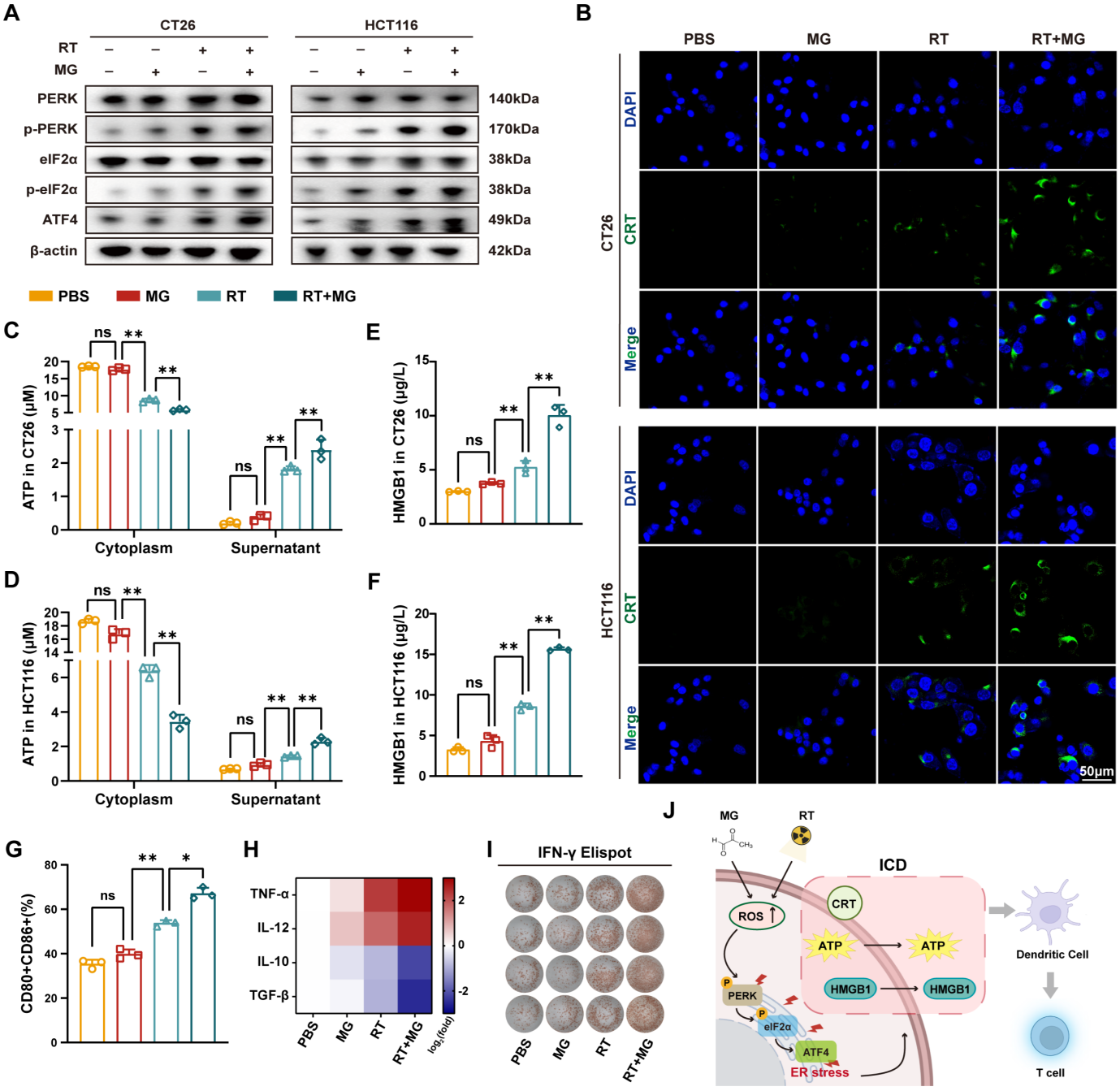

Figure 3 Methylglyoxal enhances radiation-induced endoplasmic reticulum (ER) stress and promotes immunogenic cell death (ICD) in tumor cells. (A) Western blot analysis of ER stress-related proteins expressed on the CT26 cells and HCT16 cells after coincubated with PBS and MG (200 μM) with or without X-ray (6 Gy). (B) Representative images of calreticulin (CRT) expression of CT26 cells and HCT116 cells after coincubated with PBS and MG (200 μM) with or without X-ray (6 Gy) (scale bar, 50 μm). Levels of extracellular and intracellular ATP for CT26 cells (C) and HCT116 cells (D) after coincubated with PBS and MG (200 μM) with or without X-ray (6 Gy) (n=3). Levels of high mobility group box 1 (HMGB1) in the cellular supernatant for CT26 cells (E) and HCT116 cells (F) after coincubated with PBS and MG (200 μM) with or without X-ray (6 Gy) (n=3). (G) Quantitative analysis of mature dendritic cells (DCs) ($CD80^+CD86^+$) in vivo in the different treatment groups. (H) Quantitative analysis of cytokines levels associated with mature DCs in the different treatment groups (n=3). (I) Representative images of interferon-gamma (IFN-γ) enzyme-linked immunospot assay in each group (n=4). (J) Schematic illustration of the promotion of DC maturation and activation of T cells through treatment-induced ICD. Data are presented as mean±SD. ns, no statistical difference. *p<0.05; **p<0.01.

MG enhances the antitumor effect of RT in vivo

To further investigate the combination effect of MG and RT, we utilized the syngeneic CT26 mouse tumor model and the human colorectal carcinoma HCT116 xenograft tumor model (figure 4A and online supplemental figure 13A). The data indicates that administering RT alone to mice in both the CT26 and HCT116 tumor models did not lead to a sustained response in tumor volume

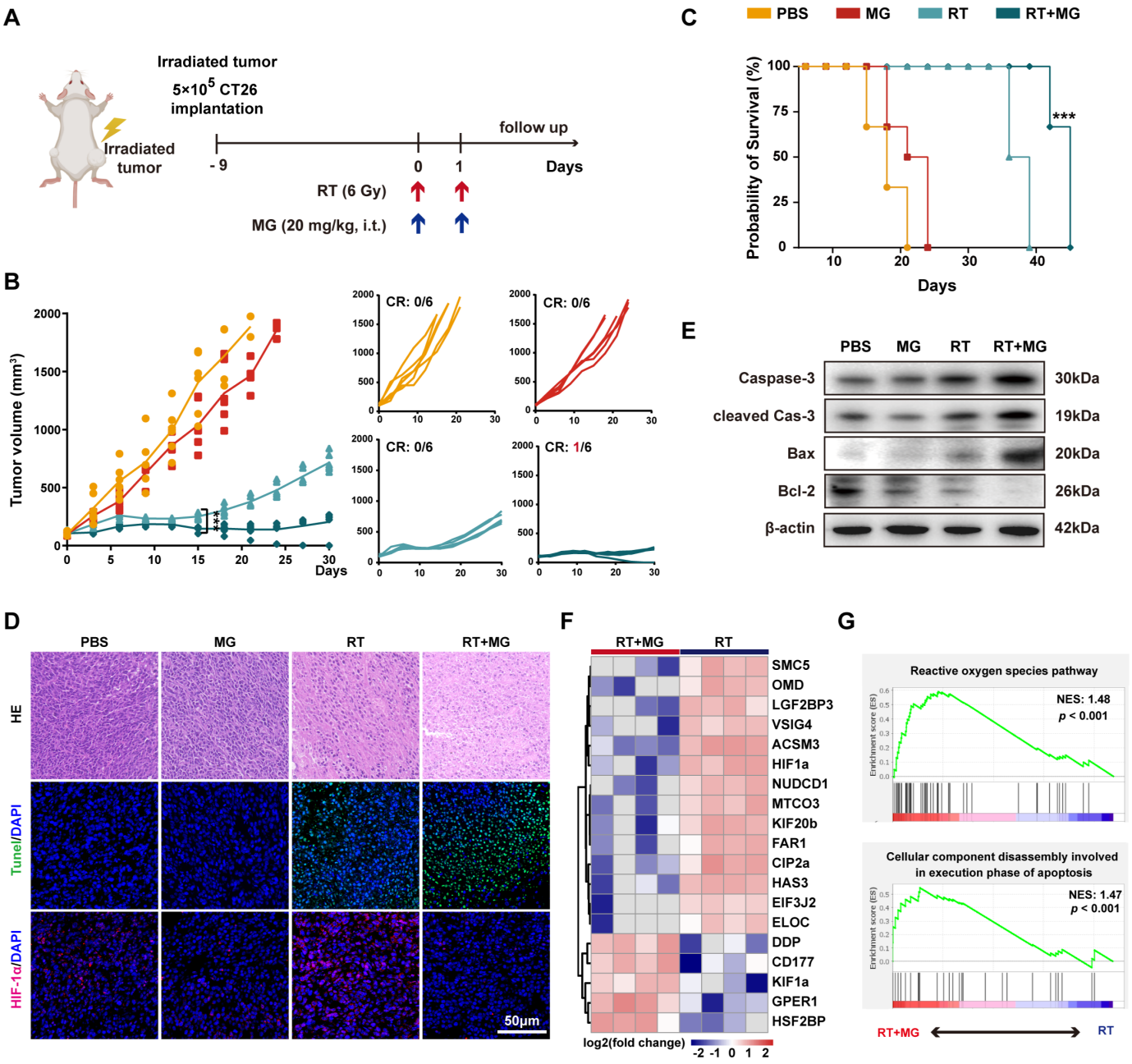

Figure 4 Methylglyoxal (MG) enhances the sensitivity of the syngeneic CT26 tumor model to radiation. (A) Workflow of the syngeneic CT26 tumor model, where MG was administered via peritumoral injection the day before a 6 Gy fraction. (B) Tumor growth curves of the syngeneic CT26 tumor model in each group, showing both the average and individual data with complete response (CR) rates (n=6). (C) Survival curves of mice after treatment (n=6). (D) Representative images of H&E staining, terminal deoxynucleotidyl transferase dUTP nick end labeling (TUNEL) assay, and hypoxia-inducible factor-alpha (HIF-α) immunofluorescence staining of syngeneic CT26 tumor model in each treatment group (scale bar, 50 μm). (E) Representative western blot images of apoptosis-related protein expressed on syngeneic CT26 tumor model treated with indicated treatments. (F) Heatmap displaying differentially expressed genes between the radiotherapy (RT) group and the RT+MG group (n=4). (G) Gene set enrichment analysis (GSEA) results based on the differentially expressed genes between the RT group and the RT+MG group. Data are presented as mean±SD. ***p<0.001.

changes (figure 4B and online supplemental figure 13B). However, by day 15, the RT+MG group had significantly lower mean tumor volume compared with the other groups in the syngeneic CT26 tumor model (p<0.05, figure 4B). Notably, one case (1/6) in the RT+MG group achieved durable CR in the syngeneic CT26 tumor model. Furthermore, the median overall survival (OS) for each group in the syngeneic CT26 tumor models was 18 days (PBS), 22.5 days (MG), 37.5 days (RT) and 45 days (RT+MG), respectively (p<0.05, figure 4C). Furthermore, two cases (2/6) in the RT+MG group of HCT116 xenograft tumor models achieved durable CR, and relatively longer OS (100% on day 48) compared with the PBS group with 31.5 days, MG group with 33 days or RT group

with 45 days, respectively (p<0.05, online supplemental figure 13B). These findings established a combined effect of the MG+RT, leading to tumor growth suppression and prolonging OS in mice.

On day 5, histological images revealed more fibrosis and necrosis in the RT+MG group compared with the RT alone (figure 4D). In addition, mice given RT+MG displayed elevated TUNEL staining with an increased level of caspase-3, cleaved Cas-3, and Bax, whereas Bcl-2 levels were downregulated compared with other groups (figure 4D,E, online supplemental figure 14A,B). Furthermore, the RT group demonstrated a significant increase in HIF-1α staining compared with the PBS group, but its levels decreased in the RT+MG group (figure 4D). These findings indicate that MG enhances radiosensitivity in vivo through the alleviation of tumor hypoxia.

Next, to further investigate the possible mechanism responsible for the radiosensitization effect of MG, we collected tumor samples from the PBS, MG, RT and RT+MG groups for transcriptome sequencing. Subsequently, we conducted GSEA analysis with the DEGs between the PBS group and MG group ($|\log_2 FC|>1$, p<0.05, online supplemental figure 15) and discovered that the genes in the MG group were notably enriched in the pathway concerning oxygen levels and apoptosis signaling pathway online supplemental figure 15B. We identified 524 DEGs in the RT+MG group compared with the RT alone ($|\log_2 FC|>1$, p<0.05, online supplemental table 7), and the top 20 DEGs were shown in figure 4F. GSEA indicated that the RT+MG group had an enrichment in pathways related to ROS and cellular component disassembly involved in apoptosis execution, compared with RT alone (figure 4G). These findings once again confirm the crucial role of ROS in the radiosensitization effect of MG.

We also assessed the biosafety of MG in vivo. As shown in online supplemental figure 16A, there was no significant difference in body weight changes among the four groups (p>0.05). Furthermore, on day 5, there was no significant increase in the levels of alanine aminotransferase (ALT), aspartate aminotransferase (AST), creatinine (CREA) and UREA (all p>0.05, online supplemental figure 16B). In addition, heart, liver, spleen, lung and kidney H&E staining revealed no additional organ toxicity 5 days after treatment online supplemental figure 16C. These findings suggest that MG has a favorable biosafety profile in vivo.

MG reshaped TiME combined with RT in vivo

RT has the potential to modulate the TiME through RT-induced ICD.[10 32] Thus, we initially examined the induction of ICD mediated via ER stress with the use of immunofluorescence staining and Western blot. The results showed that RT+MG treatment upregulated p-PERK, p-eIF2α and ATF4 compared with the other groups (figure 5A and online supplemental figure 17A,B). Additionally, we observed increased CRT exposure and HMGB1 upregulation after being treated with RT+MG (figure 5A,B and online supplemental figure 17A,B). Meanwhile, the activation of the cGAS-STING pathway mediated by RT can induce an immune response.[10 33] We found that the combination of MG and RT led to an increase in γ-H2AX staining and upregulated p-STING, p-IRF3, p-TBK1, and γ-H2AX protein (figure 5C and online supplemental figure 18A,B). Immunofluorescence staining and Western blot also confirmed the elevation of PD-L1 on tumor cells after RT+MG treatment (figure 5B, C and online supplemental figure 18A,B). These findings suggest that MG enhances the activation of the cGAS-STING pathway induced by RT in vivo.

To further evaluate the effect of RT and MG on the TiME, we utilized FCM and immunofluorescence staining to assess immunocyte infiltration in tumors, and used ELISA Kit to measure cytokines within the tumor. Our results showed that the RT+MG group exhibited a significantly higher proportion of mDCs (60.60%±1.70%) compared with the RT alone group (45.78%±2.95%) (p<0.05, figure 5D, online supplemental figure 19A). Similarly, we observed a 44.23% increase in the proportion of $CD3^+CD8^+$ T cells and a 20.37% increase in the proportion of NK cells, as well as enhanced CD8 and IFN-γ staining (figure 5E–G, online supplemental figure 19B,C). On the contrary, we observed a noticeable increase in Foxp3 staining in tumors treated with RT or RT+MG (figure 5G). We also noticed an enriched presence of Tregs infiltrating the tumors when compared with the PBS group online supplemental figures 5I,20. ELISA assays showed a significant increase in antitumor cytokines such as IFN-γ, IFN-α, IFN-β, TNF-α, and C-X-C motif chemokine ligand (CXCL)10 in the RT+MG group compared with the other groups online supplemental figures 5H,21. Whereas, protumor cytokines of IL-4, IL-6, IL-1β, IL-10, and TGF-β were found in higher levels in the tumor of the RT+MG group compared with the PBS group online supplemental figures 5H,21. These findings suggest that the combination of RT and MG reshaped the TiME in the syngeneic CT26 tumor model.

To further confirm the immunomodulatory role of RT+MG, we conducted transcriptome sequencing on tumor samples. We discovered 318 DEGs in the RT+MG group when compared with the PBS group ($|\mathrm{Log}_2 FC|>1$, p<0.05, online supplemental figure 23), (online supplemental table 8). The GSEA analysis indicated enriched signaling pathways for cytosolic DNA-sensing and cellular response to type I interferon in the RT+MG group compared with the PBS group (figure 5J). Both pathways are associated with the cGAS-STING pathway. Immune-related signaling pathways were screened in the RT+MG group and summarized in figure 5K. These results indicated the remodeling effect of RT and MG on the TiME.

MG improves the treatment and abscopal effect of iRT

Our above data has indicated that combining MG and RT may result in elevated infiltration of $CD8^+$T and NK cells compared with RT alone, showing potential for enhancing response to iRT. In addition, αPD-1

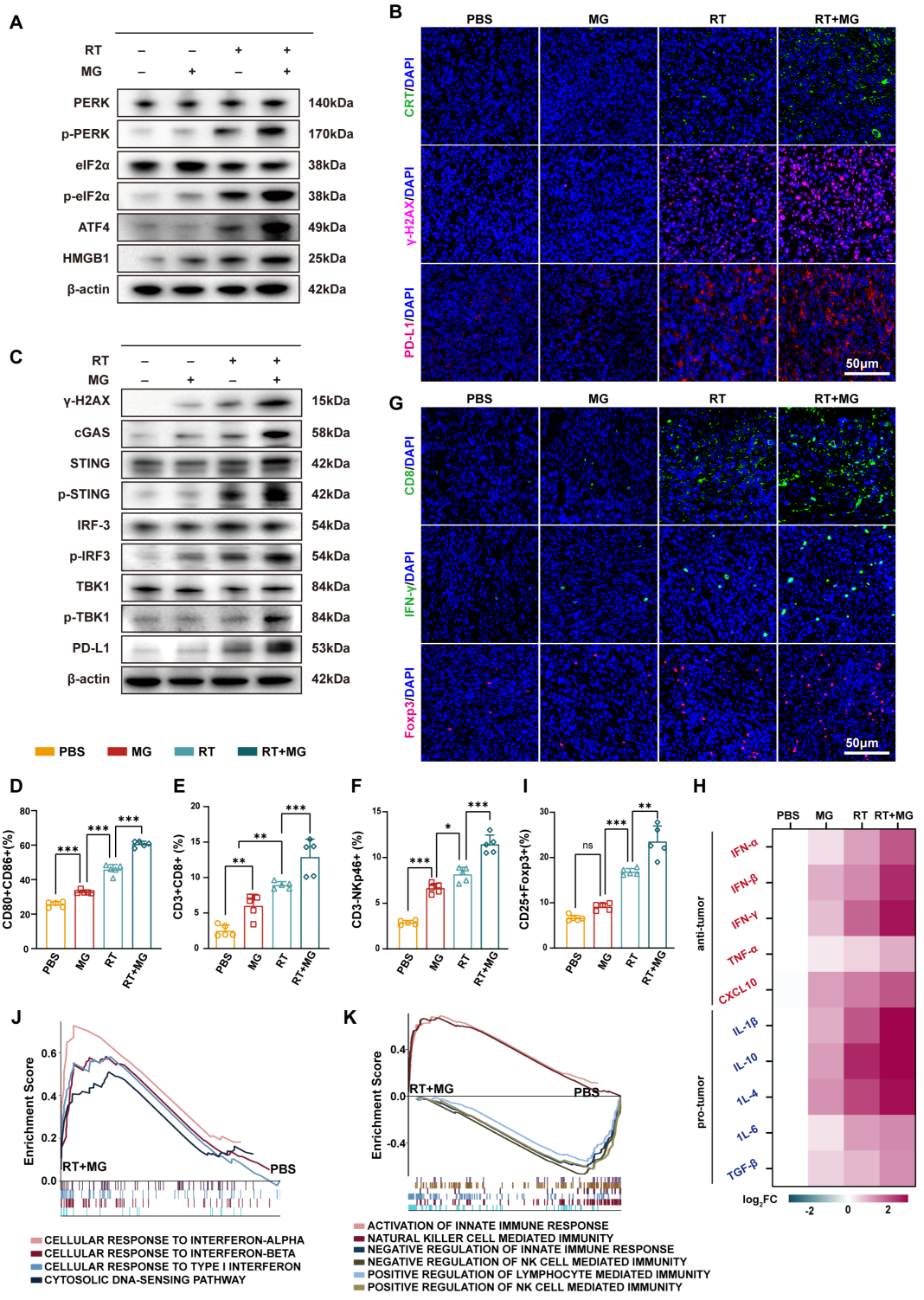

Figure 5 Bilateral effects of methylglyoxal (MG) on radiotherapy (RT)-induced immunogenic cell death (ICD) and tumor-immune microenvironment (TiME) remodeling in syngeneic CT26 tumor model. (A) Representative Western blot images showing ER stress-related proteins expressed on of syngeneic CT26 tumor model treated with indicated treatments. (B) Representative immunofluorescence staining images of calreticulin (CRT), γ-H2AX, and programmed death-ligand 1 (PD-L1) in each group (scale bar, 50 μm). (C) Representative Western blot images of cyclic guanosine monophosphate AMP synthase (cGAS)-stimulator of interferon genes (STING) pathway-related proteins expressed on of syngeneic CT26 tumor model treated with indicated treatments. Flow cytometry analysis of tumor-infiltrating dendritic cell (DC) cells (D), $CD8^+$ T cells (E), natural killer (NK) cells (F) and regulatory T (Treg) cells (I) 5 days after treatment (n=5). (G) Representative immunofluorescence staining images of CD8, interferon-gamma (IFN-γ), and Foxp3 in each group (n=5, scale bar, 50 μm). (H) Heatmap illustrating the levels of antitumor and protumor cytokines in tumor tissues 5 days after treatment (n=5). (J,K) Gene set enrichment analysis (GSEA) results comparing the PBS group and RT+MG group based on the differentially expressed genes. Data are presented as mean±SD (n=5). ns, no statistical difference. *p<0.05; **p<0.01; ***p<0.001.

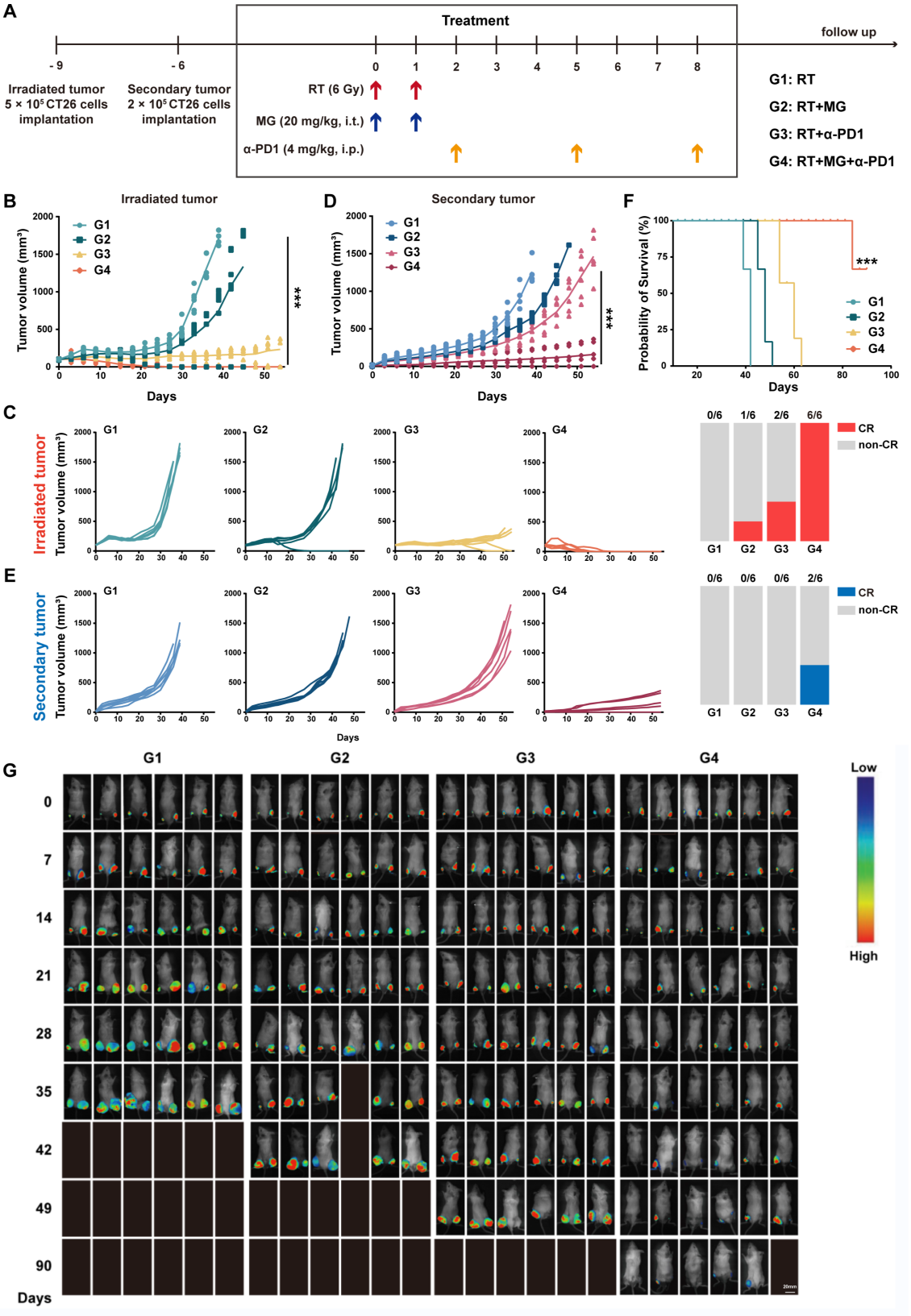

Figure 6 Evaluation of the antitumor activity of methylglyoxal (MG), radiotherapy (RT), and anti-PD1 (α-PD1) triple therapy. (A) Experimental workflow of the abscopal effect model, where α-PD1 was administered through a peritumoral injection every 3 days following RT and MG treatment. Average (B) and individual (C) tumor growth curves of the irradiated tumor in each treatment group, including complete response (CR) rates (n=6). Average (D) and individual (E) tumor growth curves of the secondary tumor in each group, also with CR rates (n=6). (F) Survival curves of mice after receiving treatment as indicated (n=6). Data are presented as mean±SD (n=5). ns, no statistical difference. ***p<0.001. (G) Bioluminescence imaging of mice in each group was conducted weekly until day 90 (n=6, scale bar, 20 mm).

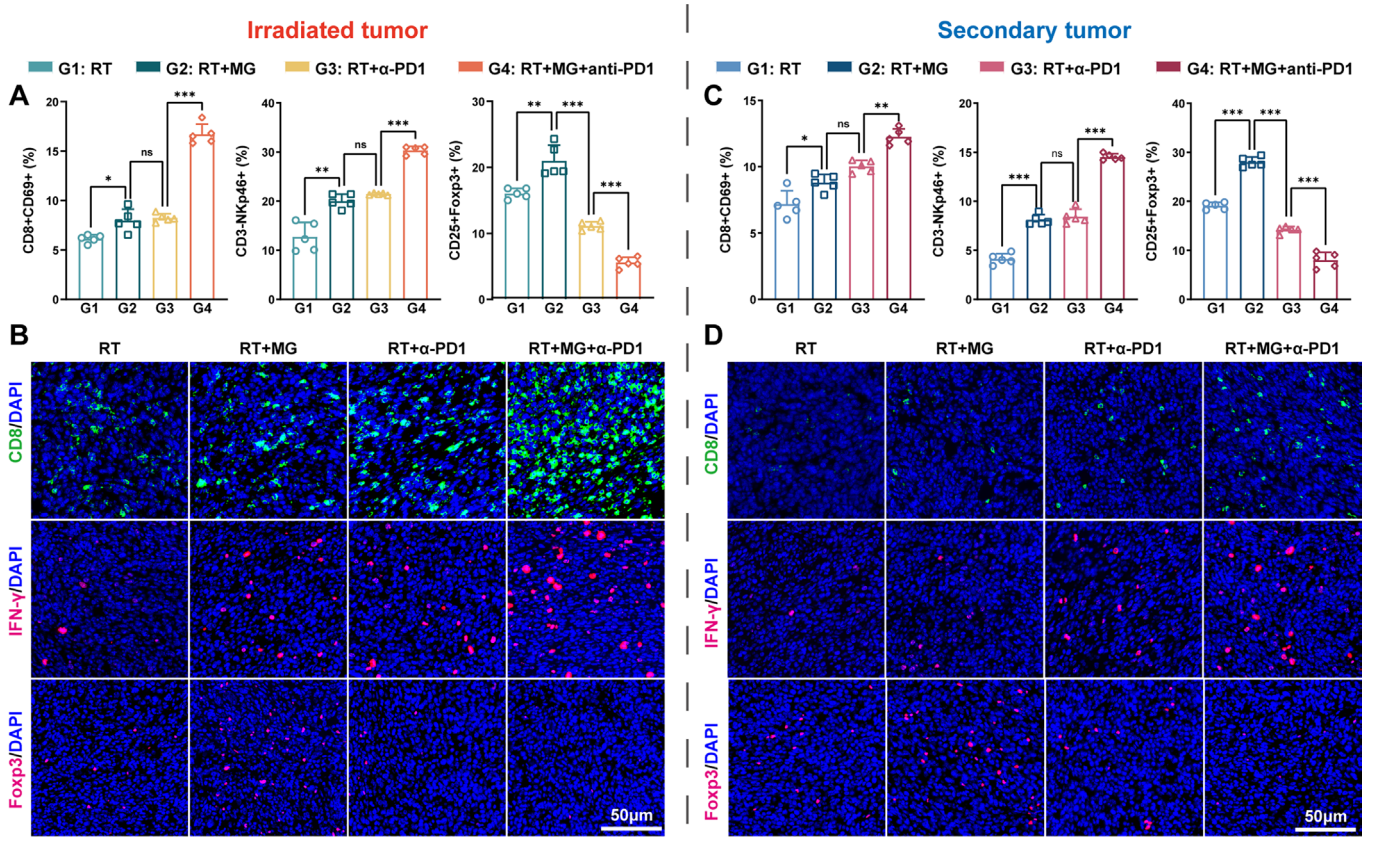

Figure 7 Reshaping of the tumor-immune microenvironment (TiME) by methylglyoxal (MG), radiotherapy (RT), and anti-PD1 (α-PD1) triple therapy. (A) The proportions of immune cells in the irradiated tumor were determined using flow cytometry (FCM) (n=5). (B) Representative images of immunofluorescence staining of CD8, Foxp3, and interferon-gamma (IFN-γ) in the irradiated tumor (scale bar, 50 µm). (C) The proportions of immune cells in the secondary tumor were determined using FCM (n=5). (D) Representative images of immunofluorescence staining of CD8, Foxp3, and IFN-γ in the secondary tumor (scale bar, 50 µm). Data are presented as mean±SD (n=5). ns, no statistical difference; *p<0.05; **p<0.01; ***p<0.001.

monotherapy demonstrated a significant antitumor effect on both primary and distant tumors in the syngeneic CT26 abscopal effect model, resulting in a longer median OS of 27 days as compared with the control group (median OS, 18 days, online supplemental figure 24). However, neither αPD-1 nor MG monotherapy effectively inhibited tumor progression. To investigate more effective treatment strategies, we, therefore, established a syngeneic CT26 abscopal effect model to assess the antitumor effects of triple therapy (MG and iRT, figure 6A). A durable CR was observed in two out of six mice in the iRT group, while all six mice were in the MG and iRT group (figure 6B,C). In the case of secondary tumors, there was a 79.2% decrease in the mean volume for the MG and iRT group compared with the iRT group on day 40 (figure 6D). Additionally, a durable CR was observed in two cases in the MG and iRT group, which strongly suggests a significant antitumor effect (figure 6E). For each group, the median OS was 42 days (RT), 28 days (RT+MG), 60 days (iRT), and for the MG+iRT group, not yet reached. The 90-day survival rate was observed to be 83.3% (p<0.05, figure 6F). Furthermore, the uniNano NIR-II real-time in vivo imaging system recorded the changes of each mouse weekly (figure 6G). The MG+iRT group displayed a higher survival rate with five out of six still alive at day 90, and two of them attained durable CR. In addition, the MG+iRT group exhibited increased fibrosis and TUNEL staining in the irradiated tumors when compared with the iRT group, including secondary tumors online supplemental figure 25. Taken together, the findings suggest that the combination of MG and iRT may hold potential for the treatment of RC.

The improvement of antitumor TiME might be the key to achieve the sustained response and enhance the abscopal effect induced by the combination of MG and iRT. To detect changes in the TiME of tumors after the treatment, we analyzed the immune cell infiltration and cytokine within tumors useing FCM and immunofluorescence, respectively. These results indicated elevated $CD8^+CD69^+$T and NK cells infiltration, as well as increased staining of IFN-γ and NKp46 in the MG+iRT group. However, there was a contradictory outcome in the infiltrated Tregs and Foxp3 staining (figure 7A,B and online supplemental figure 26). Comparable outcomes were observable in the secondary tumors (figure 7C,D and online supplemental figure 26). These findings suggest that triple therapy improves the TiME, which is vital for

generating a strong and long-lasting antitumor immune response.

DISCUSSION

To date, little attention has been paid to the correlation between the response to preRT and the gut microbiota metabolism.[19 20 38] In this study, we initially discovered a metabolism of gut microbiota (MG) that had a close relationship with preRT response. Subsequently, we demonstrated that MG could not only amplify the radiosensitivity response of RC both in vitro and in vivo but also reshape the TiME by inducing ICD and activating the cGAS-STING pathway. In addition, we have demonstrated that MG improves both the iRT response and abscopal effect in a bilateral tumor model.

In recent years, there has been an increased focus on exploring small molecules, including natural metabolites, to enhance radiosensitization in both preclinical and clinical studies.[20 39] This study identified a gut microbiota-related metabolite, MG, that could predict the response to preRT with an AUC of 0.812. MG increases ROS production in tumors by depleting GSH and inhibiting lung tumor growth, as demonstrated by Luengo A *et al*.[40] Moreover, MG could enhance the sensitivity of chemotherapy by interfering with the balance of ROS in tumors and impacting glucose metabolism's oxidative respiratory chins.[41] Our study showed that MG increased ROS production and reduced tumor hypoxia under RT conditions both in vitro and in vivo. The biochemical assay of blood samples and H&E of fetal organs confirmed the biological safety of using MG with RT. Therefore, we have determined that MG has the potential to be a promising potential radiosensitizer for RC, but requires further validation.

Previous studies have indicated that RT can modulate the TiME, rendering it a potential complement to ICIs.[10 33] As corroborated by previous findings,[14 33] our study showed that increased γ-H2AX, due to ROS, could activate the cGAS-STING pathway both in vitro and in vivo. This leads to the activation of the innate immune system in the TiME, especially the activation of NK cells.[10] Consistent with previous studies by Guo *et al*.[34] and Mehrotra *et al*,[42] our research also observed increased ROS levels inducing ER stress in this study. This ER stress, in turn, facilitated radiation-induced ICD and stimulated the activation of $CD8^+$T cells by DCs in syngeneic CT26 tumor models. RT-induced cell death generates tumor antigens,[32 35] and the presence of microbial-associated molecular patterns from gut microbiota triggers systemic immunity.[21 23] The immune-inflamed microenvironment boosts robust antitumor responses against cancerous cells.[43] However, increased ICD and activated cGAS-STING induced by RT and MG may also lead to increased infiltration of Tregs, alongside elevated levels of suppressive cytokines and upregulated expression of PD-L1, as previously reported.[44 45] We, therefore, conclude that RT and MG have the potential to reshape the TiME and enhance the efficacy of α-PD1 therapy.

ICIs have become the standard therapy for various malignancies, but the response rate remains around 20%.[12] The lack of infiltrated immune cells might be one of the key factors of this failure,[10 14] as well as the dysfunction of immune cells.[10 12] RT has the potential to recruit cytotoxic $CD8^+$T cells and NK cells into tumors,[46] and in this study combination of MG and RT resulted in stronger intraltumoral inflammations characterized by the presence of immune cells and inflammatory cytokines. This provides a more favorable scenario for immunotherapy. Meanwhile, the upregulation of PD-L1 by RT and MG supports its combination with α-PD1 therapy. α-PD1 disrupts the interaction between PD-1 and PD-L1 thereby restoring the functionality of previously inhibited CD8+ T cells[47], and reducing the infiltrated Tregs.[10 47] Our study demonstrated that combining MG with iRT not only reduced the Tregs infiltration in tumors but also increased functional $CD8^+$ T cells presence in the TiME. This improvement in TiME finally led to durable CR in all irradiated sites with prolonged OS. In addition, the TiME in the secondary tumors was also improved, which resulted in an enhanced abscopal effect (50%).

In conclusion, we have identified a gut microbiota metabolite, MG, which can reverse the radioresistance of RC by increasing ROS production and reducing tumor hypoxia. Furthermore, we have found that MG also intensifies the RT-mediated modulation of TiME by activating the cGAS-STING pathway and inducing ICD. Finally, we found that triple therapies of RT, MG, and anti-PD1 result in excellent local control and an amplified abscopal effect. Overall, this study emphasizes the potential of combining MG with iRT to enhance the immune response against tumors and improve treatment outcomes for RC. However, further studies are needed to optimize this therapeutic strategy for clinical translation applications.

Author affiliations
[1]Department of Radiation Oncology, College of Clinical Medicine for Oncology, Fujian Medical University & Fujian Cancer Hospital, Fuzhou, Fujian, China
[2]Department of Clinical Oncology, The University of Hong Kong-Shenzhen Hospital, Shenzhen, China
[3]Department of Oncology, the Second Affiliated Hospital of Nanchang University, Nanchang, Jiangxi, China
[4]The United Innovation of Mengchao Hepatobiliary Technology Key Laboratory of Fujian Province, Mengchao Hepatobiliary Hospital of Fujian Medical University, Fuzhou, China
[5]Department of Hepatopancreatobiliary Surgery, First Affiliated Hospital of Fujian Medical University, Fuzhou, Fujian, China
[6]School of Biomedical Engineering, Shanghai Jiao Tong University, Shanghai, China
[7]Department of Radiation, Mengchao Hepatobiliary Hospital of Fujian Medical University, Fuzhou, Fujian, China

Contributors HZ and LW: Conceptualization, methodology, data curation, writing - original draft. ZL and CJ: methodology, resources, data curation. XC: validation, formal analysis, data curation. KW and LL: methodology, resources. LS: investigation, resources, data curation. JP: writing - review and editing, visualization. JL: conceptualization, visualization. DZ and JW: conceptualization, writing - review and editing, visualization, project administration, funding acquisition. JW: responsible for the overall content.

Funding This research was funded by the Fujian Province Natural Science Foundation (No. 2021J01433, 2021J01438 and 2022J01433), the Fujian Province Joint Funds for the Innovation of Science and Technology (2021Y9216 and 2021Y9202). Fujian Provincial Clinical Research Center for Cancer Radiotherapy and Immunotherapy (2020Y2012), Fujian Clinical Research Center for Radiation and Therapy of Digestive, Respiratory and Genitourinary Malignancies (2021Y2014), National Clinical Key Specialty Construction Program, Startup Fund for Scientific Research, Fujian Medical University (grant number 2020QH2043), Fujian Province Outstanding Youth Science Fund Projects (2022J06034); Natural Foundation of Fujian Province, Fujian Research and Training Grants for Young and Middle-aged Leaders in Healthcare.

Competing interests No, there are no competing interests.

Patient consent for publication Not applicable.

Ethics approval All studies involving human participants were approved by the Ethics Committee of Fujian Cancer Hospital (No. SQ2021-079-01). Participants gave informed consent to participate in the study before taking part.

Provenance and peer review Not commissioned; externally peer reviewed.

Data availability statement Data are available upon reasonable request.

ORCID iD

Han Zhou http://orcid.org/0000-0002-2051-600X

REFERENCES

1 Benson AB, Venook AP, Al-Hawary MM, *et al*. Rectal cancer, version 2.2022, NCCN clinical practice guidelines in oncology. *J Natl Compr Canc Netw* 2022;20:1139–67.
2 Oronsky B, Reid T, Larson C, *et al*. Locally advanced Rectal cancer: the past, present, and future. *Semin Oncol* 2020;47:85–92.
3 Hoendervangers S, Couwenberg AM, Intven MPW, *et al*. Comparison of pathological complete response rates after Neoadjuvant short-course radiotherapy or Chemoradiation followed by delayed surgery in locally advanced Rectal cancer. *Eur J Surg Oncol* 2018;44:1013–7.
4 Li J, Ji J, Cai Y, *et al*. Preoperative concomitant boost intensity-modulated radiotherapy with oral Capecitabine in locally advanced mid-low Rectal cancer: a phase II trial. *Radiother Oncol* 2012;102:4–9.
5 Petrelli F, Trevisan F, Cabiddu M, *et al*. Total Neoadjuvant therapy in Rectal cancer: A systematic review and meta-analysis of treatment outcomes. *Ann Surg* 2020;271:440–8.
6 Saraf A, Roberts HJ, Wo JY, *et al*. Optimal Neoadjuvant strategies for locally advanced Rectal cancer by risk assessment and tumor location. *J Natl Compr Canc Netw* 2022;20:1177–84.
7 Kamran SC, Lennerz JK, Margolis CA, *et al*. Integrative molecular characterization of resistance to Neoadjuvant Chemoradiation in Rectal cancer. *Clin Cancer Res* 2019;25:5561–71.
8 Kabakov AE, Yakimova AO. Hypoxia-induced cancer cell responses driving Radioresistance of hypoxic tumors: approaches to targeting and Radiosensitizing. *Cancers (Basel)* 2021;13:1102.
9 Chen Z, Han F, Du Y, *et al*. Hypoxic Microenvironment in cancer: molecular mechanisms and therapeutic interventions. *Signal Transduct Target Ther* 2023;8:70.
10 Zhang Z, Liu X, Chen D, *et al*. Radiotherapy combined with Immunotherapy: the dawn of cancer treatment. *Sig Transduct Target Ther* 2022;7.
11 Kothari A, White MG, Peacock O, *et al*. Pathological response following Neoadjuvant Immunotherapy in mismatch repair-deficient/Microsatellite instability-high locally advanced, non-metastatic colorectal cancer. *Br J Surg* 2022;109:489–92.
12 Xu L, Zou C, Zhang S, *et al*. Reshaping the systemic tumor immune environment (STIE) and tumor immune Microenvironment (TIME) to enhance Immunotherapy efficacy in solid tumors. *J Hematol Oncol* 2022;15:87.
13 Shamseddine A, Zeidan YH, El Husseini Z, *et al*. Efficacy and safety-in analysis of short-course radiation followed by mFOLFOX-6 plus Avelumab for locally advanced Rectal adenocarcinoma. *Radiat Oncol* 2020;15:233.
14 Galluzzi L, Aryankalayil MJ, Coleman CN, *et al*. Emerging evidence for adapting radiotherapy to Immunotherapy. *Nat Rev Clin Oncol* 2023;20:543–57.
15 Gounder MM, Zhu G, Roshal L, *et al*. Immunologic correlates of the Abscopal effect in a Smarcb1/Ini1-negative poorly differentiated Chordoma after Ezh2 inhibition and radiotherapy. *Clin Cancer Res* 2019;25:2064–71.
16 Postow MA, Callahan MK, Barker CA, *et al*. Immunologic correlates of the Abscopal effect in a patient with Melanoma. *N Engl J Med* 2012;366:925–31.
17 Hanahan D. Hallmarks of cancer: new dimensions. *Cancer Discov* 2022;12:31–46.
18 Yi Y, Shen L, Shi W, *et al*. Gut Microbiome components predict response to Neoadjuvant Chemoradiotherapy in patients with locally advanced Rectal cancer: A prospective, longitudinal study. *Clin Cancer Res* 2021;27:1329–40.
19 Yang Q, Wang B, Zheng Q, *et al*. A review of gut Microbiota-derived metabolites in tumor progression and cancer therapy. *Adv Sci (Weinh)* 2023;10:2207366.
20 Teng H, Wang Y, Sui X, *et al*. Gut Microbiota-mediated nucleotide synthesis attenuates the response to Neoadjuvant Chemoradiotherapy in Rectal cancer. *Cancer Cell* 2023;41:124–38.
21 Kiousi DE, Kouroutzidou AZ, Neanidis K, *et al*. The role of the gut Microbiome in cancer Immunotherapy: Current knowledge and future directions. *Cancers (Basel)* 2023;15:2101.
22 Lozenov S, Krastev B, Nikolaev G, *et al*. Gut Microbiome composition and its metabolites are a key regulating factor for malignant transformation, metastasis and antitumor immunity. *Int J Mol Sci* 2023;24:5978.
23 Luu M, Schütz B, Lauth M, *et al*. The impact of gut Microbiota-derived metabolites on the tumor immune Microenvironment. *Cancers (Basel)* 2023;15:1588.
24 Gomes S, Rodrigues AC, Pazienza V, *et al*. Modulation of the tumor Microenvironment by Microbiota-derived short-chain fatty acids: impact in colorectal cancer therapy. *Int J Mol Sci* 2023;24:5069.
25 Hisamoto S, Shimoda S, Harada K, *et al*. Hydrophobic bile acids suppress expression of Ae2 in biliary epithelial cells and induce bile duct inflammation in primary biliary cholangitis. *J Autoimmun* 2016;75:150–60.
26 Chrysostomou D, Roberts LA, Marchesi JR, *et al*. Gut Microbiota modulation of efficacy and toxicity of cancer chemotherapy and Immunotherapy. *Gastroenterology* 2023;164:198–213.
27 Hatae R, Chamoto K, Kim YH, *et al*. Combination of host immune metabolic biomarkers for the PD-1 blockade cancer Immunotherapy. *JCI Insight* 2020;5:e133501.
28 Jiang H, Zhao P, Feng J, *et al*. Effect of Paris Saponin I on Radiosensitivity in a Gefitinib-resistant lung adenocarcinoma cell line. *Oncol Lett* 2014;7:2059–64.
29 Leu J-D, Lin S-T, Chen C-T, *et al*. Bpr0C261, an analogous of Microtubule disrupting agent D-24851 enhances the Radiosensitivity of human non-small cell lung cancer cells via P53-dependent and P53-independent pathways. *Int J Mol Sci* 2022;23:14083.
30 Gong L, Zhang Y, Liu C, *et al*. Application of Radiosensitizers in cancer radiotherapy. *Int J Nanomedicine* 2021;16:1083–102.
31 Srinivas US, Tan BWQ, Vellayappan BA, *et al*. ROS and the DNA damage response in cancer. *Redox Biol* 2019;25:101084.
32 Kroemer G, Galassi C, Zitvogel L, *et al*. Immunogenic cell stress and death. *Nat Immunol* 2022;23:487–500.
33 Kwon J, Bakhoum SF. The cytosolic DNA-sensing cGAS-STING pathway in cancer. *Cancer Discov* 2020;10:26–39.
34 Feng X, Lin T, Chen D, *et al*. Mitochondria-associated ER stress evokes Immunogenic cell death through the ROS-PERK-Eif2A pathway under PTT/CDT combined therapy. *Acta Biomater* 2023;160:211–24.
35 Krysko DV, Garg AD, Kaczmarek A, *et al*. Immunogenic cell death and damps in cancer therapy. *Nat Rev Cancer* 2012;12:860–75.
36 Wang Y, Zhao Q, Zhao B, *et al*. Remodeling tumor-associated neutrophils to enhance Dendritic cell-based HCC Neoantigen Nano-vaccine efficiency. *Adv Sci (Weinh)* 2022;9:2105631.

37 Lamberti MJ, Nigro A, Mentucci FM, *et al*. Dendritic cells and Immunogenic cancer cell death: A combination for improving antitumor immunity. *Pharmaceutics* 2020;12:256.
38 Sun Y, Zhang X, Jin C, *et al*. Prospective, longitudinal analysis of the gut Microbiome in patients with locally advanced Rectal cancer predicts response to Neoadjuvant concurrent Chemoradiotherapy. *J Transl Med* 2023;21.
39 Efimova EV, Appelbe OK, Ricco N, *et al*. O-Glcnacylation enhances double-strand break repair, promotes cancer cell proliferation, and prevents therapy-induced Senescence in irradiated tumors. *Mol Cancer Res* 2019;17:1338–50.
40 Luengo A, Abbott KL, Davidson SM, *et al*. Reactive metabolite production is a Targetable liability of Glycolytic metabolism in lung cancer. *Nat Commun* 2019;10:5604.
41 Roy A, Ahir M, Bhattacharya S, *et al*. Induction of mitochondrial apoptotic pathway in triple negative breast carcinoma cells by Methylglyoxal via generation of reactive oxygen species. *Mol Carcinog* 2017;56:2086–103.
42 Chakraborty P, Parikh RY, Choi S, *et al*. Carbon Monoxide activates PERK-regulated Autophagy to induce Immunometabolic Reprogramming and boost antitumor T-cell function. *Cancer Res* 2022;82:1969–90.
43 Denk D, Greten FR. Inflammation: the Incubator of the tumor Microenvironment. *Trends Cancer* 2022;8:901–14.
44 Li S, Mirlekar B, Johnson BM, *et al*. STING-induced regulatory B cells compromise NK function in cancer immunity. *Nature* 2022;610:373–80.
45 Zhang X, Zhang H, Zhang J, *et al*. The paradoxical role of radiation-induced cGAS-STING signalling network in tumour immunity. *Immunology* 2023;168:375–88.
46 Greten FR, Grivennikov SI. Inflammation and cancer: triggers, mechanisms, and consequences. *Immunity* 2019;51:27–41.
47 Ji D, Song C, Li Y, *et al*. Combination of radiotherapy and suppression of Tregs enhances Abscopal antitumor effect and inhibits metastasis in Rectal cancer. *J Immunother Cancer* 2020;8:e000826.